Electronic Supplementary Material (ESI) for Energy & Environmental Science.

Supplementary Information

Solar thermal-driven capacitance enhancement of supercapacitors

Fang Yi,[a†] Huaying Ren,[a†] Keren Dai,[b†] Xiaofeng Wang,[b] Yingzhou Han,[b] Kexin Wang,[a] Ke Li,[c] Baolu Guan,[d] Jie Wang,[e] Miao Tang,[a] Jingyuan Shan,[a] Hao Yang,[a] Mingsheng Zheng,[f] Zheng You,[b] Di Wei,[c*] and Zhongfan Liu[a,c*]

[a] Center for Nanochemistry, Beijing Science and Engineering Center for Nanocarbons, Beijing National Laboratory for Molecular Sciences, College of Chemistry and Molecular Engineering, Peking University, Beijing 100871, China. *Email: zfliu@pku.edu.cn*.

[b] Department of Precision Instrument, Center for Flexible Electronics Technology, Tsinghua University, Beijing 100084, P.R.China.

[c] Beijing Graphene Institute, Beijing 100095, P. R. China. *Email: weidi-cnc@pku.edu.cn*.

[d] Key Laboratory of Opto-electronics Technology, Ministry of Education, College of Electronic Science and Technology, Faculty of Information Technology, Beijing University of Technology, Beijing 100022, P. R. China.

[e] Beijing Institute of Nanoenergy and Nanosystems, Chinese Academy of Sciences, National Center for Nanoscience and Technology, Beijing 100083, China.

[f] College of Biological and Chemical Engineering, University of Science and Technology Beijing, Beijing 100083, P. R. China

[†] These authors contributed equally to this work.

Note S1. Calculation of the solar thermal conversion efficiency.

The solar thermal conversion efficiency is defined as the ratio of thermal energy originated from solar irradiation per unit time ($\dot{Q}_{in}$) to the intensity of irradiation per unit time ($\dot{q}_0$):

$$\eta_{st}=\frac{\dot{Q}_{in}}{\dot{q}_0} \tag{S1}$$

The solar thermal conversion of the supercapacitor was measured by illuminating the supercapacitor sample that was put on a thermal insulating foam. The energy balance of the entire system can be described as[1-3]

$$\sum m_i C_{p,i}\frac{dT}{dt} = \dot{Q}_{in} - \dot{Q}_{surr,out} \tag{S2}$$

where m_i and $C_{p,i}$ are the mass and specific heat capacity of the supercapacitor components respectively.

For our supercapacitor sample,

$$\sum m_i C_{p,i} = (m_{graphene}C_{p,graphene} + m_{PEDOT}C_{p,PEDOT} + m_{electrolyte}C_{p,electrolyte}) \tag{S3}$$

and the heat dissipation term, $\dot{Q}_{surr,out}$, is depicted as

$$\dot{Q}_{surr,out} = hA(T - T_{surr}) \tag{S4}$$

where T_{surr} is the surrounding temperature, h is a heat-transfer coefficient, and A is the surface area of the supercapacitor for heat dissipation.

When the surface temperature of the supercapacitor increases to the equilibrium value by solar illumination, the solar-induced energy input equals to the energy transferred out of the system:

$$\dot{Q}_{in} = \dot{Q}_{surr,out} = hA(T_{max} - T_{surr}) \tag{S5}$$

Substituting equation (S5) into equation (S1) yields:

$$\eta_{st} = \frac{hA(T_{max} - T_{surr})}{\dot{q}_0} \tag{S6}$$

A system time constant τ_s is introduced as

$$\tau_s = \frac{\sum m_i C_{p,i}}{hA} \tag{S7}$$

The temperature that increases as a function of time during the solar irradiation can be expressed as[4]

$$\frac{T_{surr} - T}{T_{surr} - T_{max}} = 1 - \exp\left(-\frac{t}{\tau_s}\right) \tag{S8}$$

and therefore τ_s can be obtained by fitting the photothermal curve data in Figure 2d.

Take the supercapacitor under solar illumination at a power density of 1 kW m^{-2} as an example, τ_s is ~38.43 s from the photothermal curve and the value of hA can be obtained from equation (S7):

$$hA = \frac{m_{graphene} C_{p,graphene} + m_{PEDOT} C_{p,PEDOT} + m_{electrolyte} C_{p,electrolyte}}{\tau_s}$$

$$= \frac{0.006\ g \times 1.34\ \mathrm{J\ kg^{-1} K^{-1}} + 0.008\ g \times 1.34\ \mathrm{J\ kg^{-1} K^{-1}} + 0.3528 g \times 5\ \mathrm{J\ kg^{-1} K^{-1}}}{38.43\ \mathrm{s}}$$

$$= 0.0464\ \mathrm{mW\ K^{-1}}$$

The T_{max} and T_{surr} are ~337.15 K (64 °C) and ~298.15 K (25 °C) respectively. The area of the illuminated supercapacitor is ~1 cm^2. Thus the solar thermal conversion efficiency of the supercapacitor is calculated to be ~18.56% under solar illumination at a power density of 1 kW m^{-2}.

Note S2. Faradaic reaction of the PEDOT:PSS in the pseudocapacitor.

The PEDOT:PSS acts as the active material for the pseudo-type supercapacitor, which provides the faradaic activity through the following doping/dedoping reaction. Note that in the reaction, A^- represents the negative ions including PSS^-, $H_2PO_4{}^-$, etc.

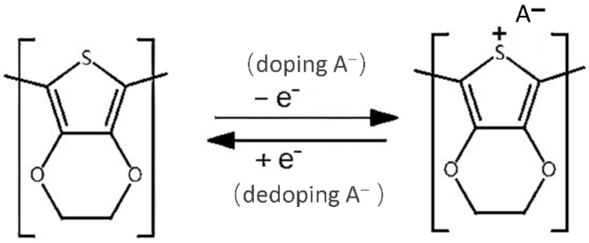

Note S3. Calculation processes of the volumetric specific capacitance.

The volumetric specific capacitances obtained from the cyclic voltammetry (CV) curves and galvanostatic charge/discharge (GCD) curves were calculated from equation (S9) and equation (S10) respectively:

$$\mathrm{C} = \frac{\int IdE}{Vv\Delta E} \tag{S9}$$

where I is the response current, ΔE is the potential window, V is the volume of the supercapacitor.

$$\mathrm{C} = \frac{i\Delta t}{V\Delta E} \tag{S10}$$

where i is the current applied for the charge/discharge, and Δt is the time elapsed for the discharge.

Note S4. Detailed explanation for the lower cyclic stability under 1 solar illumination.

The lower cyclic stability of the supercapacitor under 1 solar illumination than that in dark may be mainly due to two reasons. The first reason is the degradation of the solid-state PVA/H_3PO_4 electrolyte at the higher temperature by 1 solar illumination. It has been found that the supercapacitors (both with and without PEDOT:PSS) suffer from capacitance loss even if they stay under 1 solar illumination or heated at 62 ℃ for 2.5 h without continuous electrochemical tests (about 8~10% capacitance loss) (Fig. S7). Note that the color of the solid-state PVA/H_3PO_4 changes from clear to light brown after kept at 62 ℃ for 2.5 h (Fig. S8a-b). Therefore the electrolyte may account for the declined capacitance. To further examine this, the SEM and fourier transform infrared spectrometer (FTIR) characterization, as well as the dielectric constant measurement of the electrolyte have been conducted. The SEM images of the supercapacitor electrode filled with solid-state PVA/H_3PO_4 electrolyte before and after 2000 continuous cycles of GCD test under 1 solar illumination or heated at 63 ℃ (note: both cyclic tests last about 4 h) show that the electrolyte fully filled the electrode, and no change has been found in the SEM mophology after the GCD cyclic test under 1 solar illumination or heated at 63 ℃ (Fig. S8c-e). The FTIR spectra of the supercapacitor electrode filled with solid-state PVA/H_3PO_4 electrolyte before and after the GCD cyclic test under 1 solar illumination or heated at 63 ℃ show that three peaks have noticeable changes, which are peaks around 980 cm^{-1}, 828 cm^{-1} and 1090 cm^{-1} (Fig. S8f). The peak around 980 cm^{-1} can be assigned to the P-O stretch in alkyl phosphates and phosphites; the peak around 828 cm^{-1} can be assigned to the P-O-C linkage; and the peak around 1090 cm^{-1} can be assigned to the C-O stretch and O-H bend.[5-8] The decreases in these there peaks indicate a loss of phosphate groups that relate to ion exchange[9-11] and intro- or intermolecular dehydration,[5,12,13] which could result in decreased capacitance. Also, it is found that there is a decrease in the dielectric constant of the solid-state PVA/H_3PO_4 electrolyte after it keeps staying under 1 solar illumination or heated at 62 ℃ for

2.5 h (Fig. S9), which could also lead to decrease in capacitance.[14] The second reason for the lower cyclic stability is that the reaction rates of side reactions increase at the increased temperature by 1 solar illumination, which could contribute to reduced capacitance.[15-18]

Note S5. Details for the modeling and simulation of the mechanism for the photothermal effect enhanced capacitance of the pseudo-type supercapacitor.

For the simulation of the pseudo-type supercapacitor, a 3D mathematical model was established. In the model, the supercapacitor has the same structure as that in the experiment, which consists of two identical 3D-h graphene porous electrodes (size of each electrode: 6 mm × 2.6 mm × 0.14 mm) in parallel, separated by a gap of 0.14 mm. The PEDOT:PSS acts as the active material and has a thickness of 5 nm, which is assumed to be evenly coated on the porous electrode. The PVA/H_3PO_4 electrolyte is treated as a liquid phase in the model, with a concentration of 1 mol/L. The diffusion coefficient in the electrode and electrolyte phase, as well as the transference number are assumed to be independent of the electrolyte concentration. The entire surface area contributes to the electric double-layer capacitance. All side reactions are neglected.

The conductivity and diffusion coefficient are modified in the electrode area considering the porosity:[19,20]

$$D_{1,ef}={\varepsilon_1}^{1.5}D_1, \quad \sigma_{1,ef}={\varepsilon_1}^{1.5}\sigma_1, \quad \sigma_{2,ef}={\varepsilon_2}^{1.5}\sigma_2 \tag{S11}$$

where $D_{1,ef}$, $\sigma_{1,ef}$, and $\sigma_{2,ef}$ are the effective diffusion coefficient of the electrolyte, the effective conductivity in the electrolyte phase, and the effective conductivity in the electrode phase, respectively. D_1, σ_1, and σ_2 are their corresponding original values. ε_1 and ε_2 are the volume fractions of the electrolyte phase and the electrode phase respectively.

The total surface current density (I_{SC}) (unit: A m^{-2}) that remains constant during the galvanostatic charge/discharge (GCD) process is the sum of the surface current density in the electrolyte phase (i_1) and the surface current density in the electrode phase (i_2):

$$I_{SC}=i_1+i_2 \tag{S12}$$

For every position in the model, the conservation of charge leads to:

$$0=\frac{\partial i_1}{\partial x}+\frac{\partial i_2}{\partial x} \tag{S13}$$

The movement of current in the electrode phase reflects the movement of electrons and the potential in the electrode phase ϕ_2 is correlated to i_2 by Ohm's law:

$$i_2 = -\sigma_{2,ef}\frac{\partial \phi_2}{\partial x} \tag{S14}$$

The movement of current in the electrolyte phase reflects the movement of ions, which are originated from the faradaic redox reaction and the double-layer charge.[21-23] Both the faradaic current $i_{v,f}$ and the double-layer current $i_{v,dl}$ contribute to the current of the supercapacitor (note that $i_{v,f}$ and $i_{v,dl}$ are the volume current densities that have the unit of A m^{-3}):

$$i_{v,f} = S_f j_f \tag{S15}$$

$$i_{v,dl} = S_d C_{dl}\frac{\partial(\phi_2 - \phi_1)}{\partial t} \tag{S16}$$

Therefore:

$$\frac{\partial i_1}{\partial x} = S_f j_f + S_d C_{dl}\frac{\partial(\phi_2 - \phi_1)}{\partial t} \tag{S17}$$

where S_f and S_d represent the specific surface area for the pseudocapacitance and double-layer capacitance per unit electrode volume, respectively. j_f is the faradaic transfer current density. C_{dl} represents the double-layer capacitance. ϕ_2 and ϕ_1 are the potential in the electrode phase and in the electrolyte phase, respectively.

The j_f can be expressed in a kinetic form using the Bulter-Volmer equation:[22,24]

$$j_f = i_0\left\{exp\left[\alpha_a\frac{nF}{RT}(\phi_2 - \phi_1 - U_1)\right] - exp\left[-\alpha_c\frac{nF}{RT}(\phi_2 - \phi_1 - U_1)\right]\right\} \tag{S18}$$

where i_0 is the exchange current density, α_a is the anodic transfer coefficient (set as 0.5), α_c is the cathodic transfer coefficient (set as 0.5), n is the number of electrons involved in the faradaic reaction (set as 1), F is Faraday's constant, R is the universal gas constant, T is the absolute temperature, and U_1 is the equilibrium potential for the faradaic reaction.

The exchange current density can be expressed as follows:[25]

$$i_0 = \mathrm{Fk}\left(c_{2,max} - c_2\right)^{\alpha_a}(c_2)^{\alpha_c}(c_1)^{\alpha_a} \tag{S19}$$

where k is the standard rate constant, c_2 is the electrode phase concentration at the surface and c_1 is the electrolyte concentration.

U_1 can be evaluated as a function of the state of charge δ,[26] and U_1 of the anode is evaluated as:

$$U_1=0.5(1+\delta) \tag{S20}$$

U_1 of the cathode is evaluated as:

$$U_1=0.5\delta \tag{S21}$$

The δ represents the degree of faradaic reaction, which can be expressed as:[25-27]

$$\delta=\frac{c_2}{c_{2,max}} \tag{S22}$$

Assuming that the transport of ions can take place on the surface and in the bulk of the active material. If considering the PEDOT:PSS film as a group of densely packed spherical particle, then a material balance inside the particles can be given by:[28]

$$\frac{\partial c_2}{\partial t}=D_2\left[\frac{\partial^2 c_2}{\partial r^2}+\frac{2}{r}\frac{\partial c_2}{\partial r}\right] \quad 0\leq r\leq r_p \tag{S23}$$

where r is the radical coordinate, r_p is the particle radius (equals to half of the film thickness), and D_2 is the diffusion coefficient of the reaction ion in the particle.

In the electrolyte phase, Ohm's law is modified considering the porosity of the electrode:[29]

$$i_1=-\sigma_{1,ef}\frac{\partial\phi_1}{\partial x}-\frac{2\sigma_{1,ef}RT}{F}(1-t_-)\frac{\partial(\ln c_1)}{\partial x} \tag{S24}$$

where t_- is the transport number. The electrolyte concentration c_1 correlates with the faradaic redox reaction and double-layer reaction via a material balance on the electrolyte using concentrated solution theory:[19]

$$\varepsilon_1\frac{\partial c_1}{\partial t}+\nabla\cdot\left(-D_{1,ef}\nabla c_1+\frac{i_1 t_-}{F}\right)=\frac{i_{v,f}+i_{v,dl}}{F} \tag{S25}$$

In the separator, the porous electrode theory is not applicable, and equation (S24) and (S25) can be simplified as:

$$i_1=-\sigma_{1,ef}\frac{\partial\phi_1}{\partial x} \tag{S26}$$

$$\frac{\partial c_1}{\partial t}+\nabla\cdot\left(-D_1\nabla c_1+\frac{i_1 t_-}{F}\right)=0 \tag{S27}$$

The boundary conditions of the model are as follows:

at x=0

$$\frac{\partial c_1}{\partial x}=0, \quad i_1=0, \quad I_{sc}=i_2 \tag{S28}$$

at x=$L_+ = L_+ + L_2$

$$i_2=0, \quad \frac{\partial i_1}{\partial x}=0 \tag{S29}$$

where L is the thickness of the electrode,

at x=$L_+ + L_2 + L_-$

$$\frac{\partial c_1}{\partial x}=0, \quad i_1=0, \quad I_{sc}=i_2, \quad \phi_2=0 \tag{S30}$$

inside the PEDOT:PSS layer

$$\left.\frac{\partial c_2}{\partial r}\right|_{r=0}=0, \quad \left.\frac{\partial c_2}{\partial r}\right|_{r=r_p}=-\frac{i_{v,f}}{D_2 F a_v} \tag{S31}$$

The initial conditions are as follows:

at t=0

$$c_1=c_0, \quad c_2=c_{20}, \quad \phi_2|_{x=0}=0 \tag{S32}$$

where c_0 is the initial electrolyte concentration and c_{20} is the initial electrode phase concentration.

In the model, the supercapacitor has an initial potential of 0 V and is set to be fully charged to 0.7 V and then discharged completely back to 0 V. The GCD current density is set as 35.7 A/m^2 (6.7 mA cm^{-3}). The equations of the model are solved by using the COMSOL Multiphysics software.

The parameters used in the simulation for the supercapacitor in dark (~25 ℃) are listed in Table S1.

Table S1. List of parameters in the simulation model for the supercapacitor in dark (298.35 K).

Parameter	Physical meaning	Value	Reference
I_{SC}	Charge/discharge current density	35.7 A/m^2	Measured
T	Absolute temperature	298.35 K	Measured
c_{2max}	Maximum concentration of active material	9.36 mol/L	Estimated
c_{20}	Initial concentration of active material	0 mol/L	Assumed
k	Reaction rate constant	2.30×10^{-10} m/s	Estimated
α_a	Anodic transfer coefficient of faradaic reaction	0.5	Assumed
α_c	Cathodic transfer coefficient of faradaic reaction	0.5	Assumed
t_-	Transport number	0.363	Assumed
σ_1	Conductivity in the electrolyte phase	66.3 S/m	Estimated
σ_2	Conductivity in the electrode phase	674.4 S/m	Estimated
D_1	Diffusion coefficient of reaction ion in the electrolyte phase	1.18×10^{-15} m^2/s	Estimated
D_2	Diffusion coefficient of reaction ion in the electrode phase	1.18×10^{-15} m^2/s	Estimated
d_p	Thickness of active material	5×10^{-9} m	Estimated
S_f	Specific surface area for the pseudocapacitance per unit electrode volume	5.6×10^5 m^2/m^3	Estimated
S_d	Specific surface area for the double-layer capacitance per unit electrode volume	5.6×10^5 m^2/m^3	Estimated
C_{dl}	Electric double-layer capacitance	2.1 F/m^2	Measured
c_1	Concentration of electrolyte	1 mol/L	Estimated
ε_1	Volume fraction of the electrolyte phase	0.75	Estimated
ε_2	Volume fraction of the electrode phase	0.25	Estimated
L_e	Gap between the two electrodes	1.4×10^{-4} m	Measured
L	Thickness of electrode	1.4×10^{-4} m	Measured
E_{size}	Size of electrode	6 mm × 2.6 mm × 0.14 mm	Measured

Note that the maximum electrode phase concentration ($c_{2,max}$) is the maximum amount of ions the active material can combine through faradaic reaction per unit volume. For our pseudo-type supercapacitor, it is the concentration when each monomer (EDOT) of PEDOT is doped with a negative ion, which can be estimated as:

$$c_{2,max} = \frac{\rho}{M} \tag{S33}$$

where ρ is the mass density of EDOT (~1.331g cm^{-3}) and M is the molar mass of EDOT (142.18 g mol^{-1}). Thus $c_{2,max}$ is ~9.36 mol L^{-1}.

Supposing that there is no temperature difference inside the supercapacitor, then the main variables in the model induced by the increasing temperature under solar illumination are the temperature T, the conductivities of the electrolyte σ_1 and the electrode σ_2, the electric double-layer capacitance C_{dl}, the diffusion coefficient D, and the reaction rate constant k.

The resistance of the electrolyte is estimated by subtracting the resistances of the two electrodes from the equivalent series resistance obtained from the electrochemical impedance spectroscopy (EIS) curve.

The electric double-layer capacitances in dark and under solar illumination are measured from the electric double-layer capacitor (EDLC) that has the same structure as the pseudo-type supercapacitor but only without the PEDOT:PSS active material.

The diffusion coefficient in the electrode phase is estimated from the cyclic voltammetry (CV) curves. During the CV process, the total current response at a fixed potential (i(V)) can be divided into the adsorption-controlled capacitive effects (proportional to the scan rate υ) and diffusion-controlled faradaic reactions (proportional to $\upsilon^{1/2}$):[30-32]

$$I(V)=I_c(V)+I_f(V)=\eta_c\upsilon+\eta_f\upsilon^{1/2} \tag{S34}$$

The values of η_c and η_f can be obtained by plotting $I_{(V=0.7\ V)}/\upsilon^{1/2}$ against $\upsilon^{1/2}$ (Fig. S23).

The peak current of the diffusion-controlled faradaic reactions ($I_{f,peak}$) can be described by the Randles-Sevcik equation:[33,34]

$$I_{f,peak} = 0.4463\,\upsilon^{1/2}\,nF\left(\frac{nF}{RT}\right)^{1/2}A_s c_{2f} D_2^{1/2} \tag{S35}$$

where υ is the scan rate, F is Faraday’s constant, R is the universal gas constant, n is the number of exchanged electron during the redox process (set as 1), A_s is the geometry area of the electrode (set as 6 mm × 2.6 mm), c_{2f} is the concentration of reaction ions in the electrode (set as 1 mol/L).

Note that there are no obvious redox peaks in the measured CV curves, which is common for supercapacitors with PEDOT:PSS as the active material because of the broad redox activity of PEDOT.[35,36] The maximum value in the CV curve ($I_{(V=0.7V)}$) can be taken as the $I_{f,peak}$, and then the diffusion coefficient can be calculated as:

$$\mathrm{D}_2 = \frac{(\frac{I_{f,peak}}{v^{1/2}})^2 RT}{0.4463^2 n^3 F^3 {A_s}^2 {c_{2f}}^2} = \frac{{\eta_f}^2 RT}{0.4463^2 n^3 F^3 {A_s}^2 {c_{2f}}^2} \tag{S36}$$

The diffusion coefficient in the electrode phase in dark is calculated to be 1.18×10^{-15} m^2/s. The diffusion coefficient in the electrolyte phase is set as the same as that in the electrode phase. It is found that the electrolyte concentration gradient increases with the charging potential and reaches the maximum value when the supercapacitor is fully charged (Fig. S18a). When changing the diffusion coefficient from 1.18×10^{-15} m^2/s to 1.18×10^{-11} m^2/s while other parameters maintained the same, the electrolyte concentration becomes more evenly distributed but the capacitance is nearly unchanged (Fig. S18).

The reaction rate constants in dark (~25°C) is estimated by using the following simplified equation:[37,38]

$$\mathrm{k} = \frac{RT}{F^2}\frac{1}{n^2 A_r c_{1f} R_{ct}} \tag{S37}$$

where A_r is the reaction area of the electrode, c_{1f} is the concentration of reaction ion in the electrolyte phase, R_{ct} is the charge transfer resistance. Considering that the accurate A_r and c_{1f} are hard to be acquired due to the complicated kinetic process, R_{ct} is inconspicuous in the EIS curve and this equation is simplified, an adjustment coefficient ξ is introduced as:

$$n^2 R_{ct} A c_{1f} = \xi\, n'^2 R'_{ct} A' c'_{1f} \tag{S38}$$

where ξ is 7.5×10^{2} and A' is the geometry area of the electrode (6 mm × 2.6 mm), n is set as 1, c'_{1f} is set as 1 mol/L. R'_{ct} is set as 100 Ω at 298.35 K (in dark). The calculated k at ~25 ℃ (in dark) is ~2.30×10^{-10} m/s.

Since the temperature of the supercapacitor from in dark to under 1 solar illumination is within a common range (25~65 ℃), van't Hoff's rule is employed to estimate the reaction rate constants at the elevated temperatures under solar illumination. According to van't Hoff's rule of the temperature effect on the equilibrium constant for a chemical reaction, the reaction rate constant increases twice to three times for every increase of 10 ℃.[39-41] Assuming that there is a twofold increase in the reaction rate constant for every increase of 10 ℃ within the temperature range of 25~65 ℃, the reaction rate constants under solar illumination are estimated as:

$$k_{solar}=2^{(T_{solar}-T_{dark})/10}\ k_{dark} \tag{S39}$$

As is mentioned above, the k in dark is estimated to be ~2.3×10^{-10} m/s. Then the k under solar illumination intensities of 0.41 kW m^{-2} (~40℃), 0.72 kW m^{-2} (~52℃) and 1 kW m^{-2} (~64℃) are calculated to be ~6.51×10^{-10} m/s, ~1.49×10^{-9} m/s and ~3.43×10^{-9} m/s, respectively.

Note that the estimated k values fit well with the Arrhenius equation (Fig. S19c):

$$k = Ae^{-E_A/RT} \tag{S40}$$

where R is the universal gas constant, A is the frequency factor (~17.123) and E_A is the actication energy (~61.534 kJ mol^{-1}).

The changed parameters for the supercapacitor under 1 solar illumination are listed in Table S2. The simulated GCD curve under 1 solar illumination has a discharging time ~1.7 times longer than that in dark, which is close to the experimental data (~1.5 times) (Fig. S20a).

Table S2. List of changed parameters in the simulation model for the supercapacitor at the photothermal temperature of 337.55 K (Solar 64℃).

Parameter	Physical meaning	Value	Reference
T	Absolute temperature	337.55 K	Measured
k	Reaction rate constant	3.43×10^{-9} m/s	Estimated
σ_1	Conductivity in the electrolyte phase	131.2 S/m	Estimated
σ_2	Conductivity in the electrode phase	720.9 S/m	Estimated
D_1	Diffusion coefficient of reaction ion in the electrolyte phase	4.90×10^{-15} m^2/s	Estimated
D_2	Diffusion coefficient of reaction ion in the electrode phase	4.90×10^{-15} m^2/s	Estimated
C_{dl}	Electric double-layer capacitance	8.6 F/m^2	Measured

To further investigate the contribution of each variable parameter to the increasing capacitance by the photothermal effect, the GCD curves were simulated by only changing an individual variable parameter and the temperature to those under 1 solar illumination based on the parameters in dark. The simulated GCD curves (Fig. S20b) show that increase in the conductivity, reaction rate constant and electric double-layer capacitance all contribute to the enhanced capacitance.

The changed parameters in the model for the supercapacitor under solar illumination intensities of 0.41 kW m^{-2} (~40℃) and 0.72 kW m^{-2} (~52℃) are shown in Table S3 and S4, respectively. The simulated GCD curves show a increasing discharging time with the increasing solar power density (Fig. S20a), which agrees with the experimental results.

Table S3. List of changed parameters in the simulation model for the supercapacitor at the photothermal temperature of 313.65 K (Solar 40℃).

Parameter	Physical meaning	Value	Reference
T	Absolute temperature	313.65 K	Measured
k	Reaction rate constant	6.51×10^{-10} m/s	Estimated
σ_1	Conductivity in the electrolyte phase	87.8 S/m	Estimated
σ_2	Conductivity in the electrode phase	678.8 S/m	Estimated
D_1	Diffusion coefficient of reaction ion in the electrolyte phase	1.87×10^{-15} m^2/s	Estimated

D_2	Diffusion coefficient of reaction ion in the electrode phase	1.87×10^{-15} m^2/s	Estimated
C_{dl}	Electric double-layer capacitance	4.54 F/m^2	Measured

Table S4. List of changed parameters in the simulation model for the supercapacitor at the photothermal temperature of 325.45 K (Solar 52℃).

Parameter	Physical meaning	Value	Reference
T	Absolute temperature	325.45 K	Measured
k	Reaction rate constant	1.49×10^{-9} m/s	Estimated
σ_1	Conductivity in the electrolyte phase	103.7 S/m	Estimated
σ_2	Conductivity in the electrode phase	696.9 S/m	Estimated
D_1	Diffusion coefficient of reaction ion in the electrolyte phase	2.99×10^{-15} m^2/s	Estimated
D_2	Diffusion coefficient of reaction ion in the electrode phase	2.99×10^{-15} m^2/s	Estimated
C_{dl}	Electric double-layer capacitance	6.82 F/m^2	Measured

Note S6. The modeling and simulation for the mechanism of the photothermal effect enhanced capacitance of the double-layer-type supercapacitor.

To investigate the mechanism for the increasing capacitance of the double-layer-type supercapacitor (EDLC) with the increasing photothermal temperature, a classic EDLC model (for plane electrodes) was applied by treating the stern and diffuse layer capacitances in series. In the model, the total double-layer integral areal capacitance C_{dl} can be expressed as:[37,42]

$$\frac{1}{C_{dl}}=\frac{1}{C_{dl}^{S}}+\frac{1}{C_{dl}^{D}}=\frac{H}{\varepsilon_0\bar{\varepsilon}_r}+\frac{\psi_D}{2zeN_Ac_\infty\lambda_D}\left\{\frac{2}{\nu_p}\ln\left[1+2\nu_p\sin h^2\left(\frac{ze\psi_D}{2k_BT}\right)\right]\right\}^{-1/2} \tag{S41}$$

where H is the thickness of the Stern layer that is approximately the radius of the solvated ions,[37,43,44] $\bar{\varepsilon}_r$ is the average dielectric permittivity along electrode surface, ε_0 is the free space permittivity, T is the absolute temperature, z is the ion valency, e is the elementary charge, N_A is the Avogadro constant, c_∞ is the bulk molar concentration of ion species, k_B is the Boltzmann constant, ψ_D is the potential at the interface located at x=H. Note that the ion conducting ability of the solid-state PVA/H_3PO_4 electrolyte is mainly due to the ion exchange properties of the phosphorylated PVA (esterification product of PVA and H_3PO_4).[9,13,45] The accurate concentration of the ion-exchange species can not be obtained since it is unable to get the exact degree of the esterification reaction between the PVA and H_3PO_4. In the simulation model, the ion concentration of the solid-state PVA/H_3PO_4 electrolyte is set as 1 mol/L (approximately the concentration of H_3PO_4 in the mixture of water, H_3PO_4 and PVA (weight ratio: 10:1:1) when preparing the PVA/H_3PO_4 electrolyte).

λ_D is the Debye length for symmetric electrolytes that corresponds to an estimated EDLC thickness,[37,43] which is defined as:

$$\lambda_D=\sqrt{\varepsilon_0\bar{\varepsilon}_rk_BT/2z^2e^2N_Ac_\infty} \tag{S42}$$

ν_p is the packing number that represents the ratio of the total bulk ion concentration to the maximum ion concentration assuming a simple cubic ion packing,[46,47] which is defined as:

$$\nu_p=16H^3N_Ac_\infty \tag{S43}$$

When the EDLC undergoes a temperature change, the variables in equation (S41) are T, $\bar{\varepsilon}_r$ and λ_D. The constant and the variable parameters at different photothermal temperatures are listed in Table S5 and S6, respectively.

Table S5. The constant parameters at different photothermal temperatures in the EDLC model.

Parameter	Value	Parameter	Value
ε_0	8.854×10^{-12} F/m	H	0.25×10^{-9} m
z	1	ψ_D	0.7 V
N_A	6.022×10^{23} mol^{-1}	e	1.602×10^{-19} C
ν_p	2.409×10^{18}	c_∞	1000 mol/m^3
k_B	1.381×10^{-23} J K^{-1}		

Table S6. The variable parameters at different photothermal temperatures in the EDLC model.

T (K)	$\bar{\varepsilon}_r$	λ_D
298.15	68959.00	9.018×10^{-9}
311.15	134702.96	1.288×10^{-8}
324.15	223502.60	1.693×10^{-8}
337.15	612261.17	2.858×10^{-8}

Note S7. Details for the simulation of the temperature distribution along the supercapacitor under solar illumination.

The solar irradiance contains ~7% of ultraviolet light, ~50% of visible light and ~43% of infrared light. In the visible region, the penetration depth of the light can be estimated as $1/\alpha$, where α is the absorbance coefficient; and α can be simply calculated as $\alpha=a/d$, where a is the absorbance and d is the thickness of the supercapacitor.[48-51] The absorbance of the supercapacitor is ~2 among the visible light range (Fig. S22a), and therefore the penetration depth of the visible light in the supercapacitor is approximately half of the supercapacitor thickness.

Supposing that the penetration depths of light over the entire light source spectrum (340~850 nm, Fig. S4b) are all half of the supercapacitor thickness, a simplified model is established by using the COMSOL Multiphysics software. The supercapacitor can be regarded as being composed of small units of 3D graphene and solid-state PVA/H_3PO_4 electrolyte. In the model, a typical cuboid material unit contains two parts with the same volume (side length of each square is set as 1 mm). The temperature of the top square part is set as the photothermal temperature induced by solar illumination while the temperature of the bottom square part is set as the temperature without solar illumination (in dark). Also, the bottom side of the bottom square part is set as thermal insulating (corresponding to the thermal insulating foam in the experiment), and the surrounding environment is set as non-circulating air. The photothermal effect induced heat will transfer from the top part to the bottom part and dissipate into the surrounding environment.

The heat transfer in the solid material can be expressed by the following equations:

$$\rho C_p \frac{\partial T}{\partial t} + \rho C_p \mathbf{u} \cdot \nabla \mathrm{T} + \nabla \cdot \mathbf{q} = \mathrm{Q} \tag{S44}$$

$$\mathbf{q} = -\mathrm{k}\nabla \mathrm{T} \tag{S45}$$

where ρ is the material density, C_p is the material heat capacity at constant pressure, k is the material thermal conductivity, $\boldsymbol{u}$ is the velocity field, and Q is the heat source.

The temperature distribution is obtained when the heat transfer and heat dissipation reach an equilibrium. The parameters in the model for the heat transfer of the 3D graphene and the solid-state PVA/H_3PO_4 electrolyte are listed in Table S7.

Table S7. Parameters used in the simulation model for the temperature distribution along the supercapacitor under 1 solar illumination.

Parameter	3D graphene	Solid PVA/H_3PO_4
ρ (kg/m3)	2.8	1200
C_p (J/(kg· K))	1.34×10^3	5×10^3
k (W/(m·k))	800	0.2

Fig. S1 TEM images and Raman spectrum of the 3D-h graphene. (a) Typical HRTEM overview of the graphene nanoplates. (b) Enlarged HRTEM view showing the thickness of a typical graphene nanoplate (~7 layered). (c) Raman spectrum of the 3D-h graphene. Note that the intensity of the 2D peak (~2690 cm^{-1}) is ~0.7 times that of the G peak (~1580 cm^{-1}).

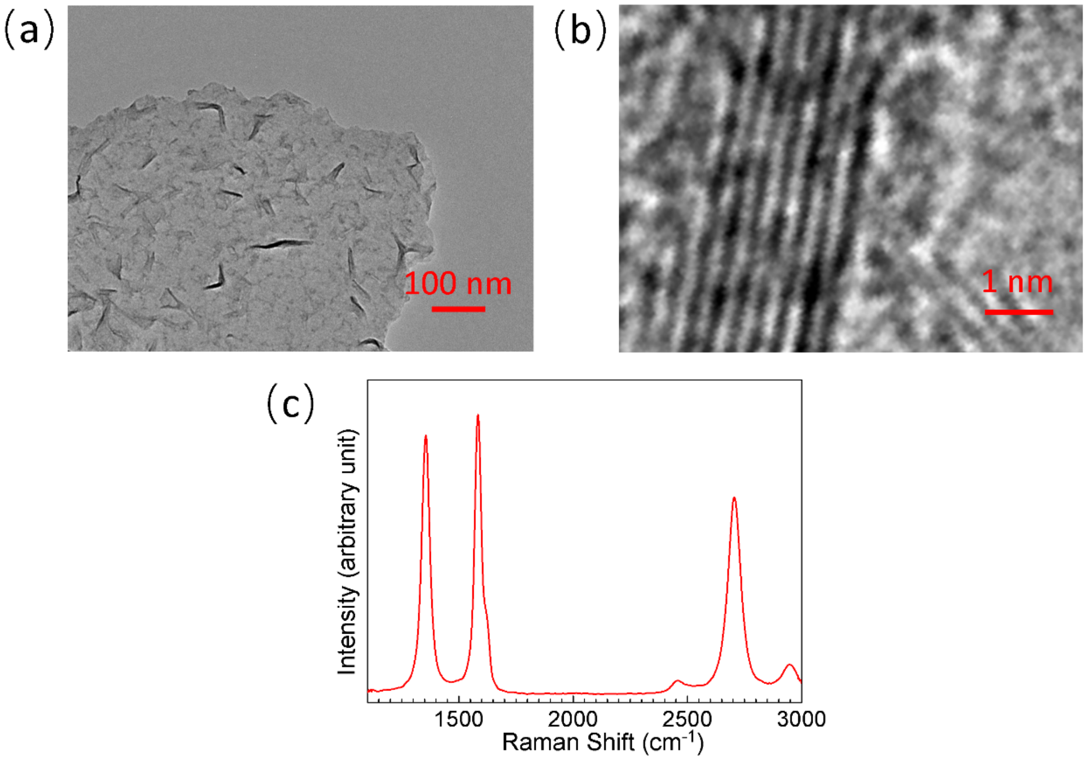

Fig. S2 SEM images of the PEDOT:PSS coated 3D-h graphene. (a) SEM overview of the 3D-h graphene coated with PEDOT:PSS. (b) Enlarged SEM view showing the thickness of the PEDOT:PSS layer.

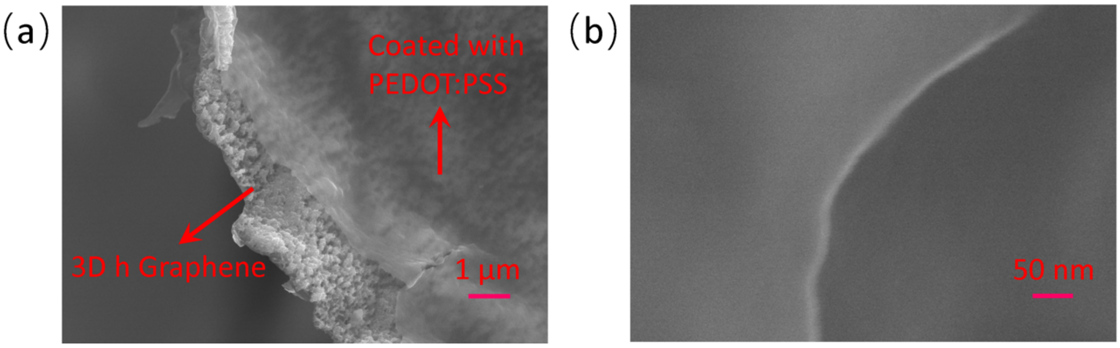

Fig. S3 Light interactions with flat surface and graphene nanoplates anchored surface. (a) Schematic depiction showing the light reflected away from the flat surface. (b) Calculated cross-sectional electric field distribution of the flat surface at light wavelength of 550 nm. (c) Schematic depiction showing the light trapped in the graphene nanoplates anchored surface. (d) Calculated cross-sectional electric field distribution of the graphene nanoplates anchored surface at light wavelength of 550 nm.

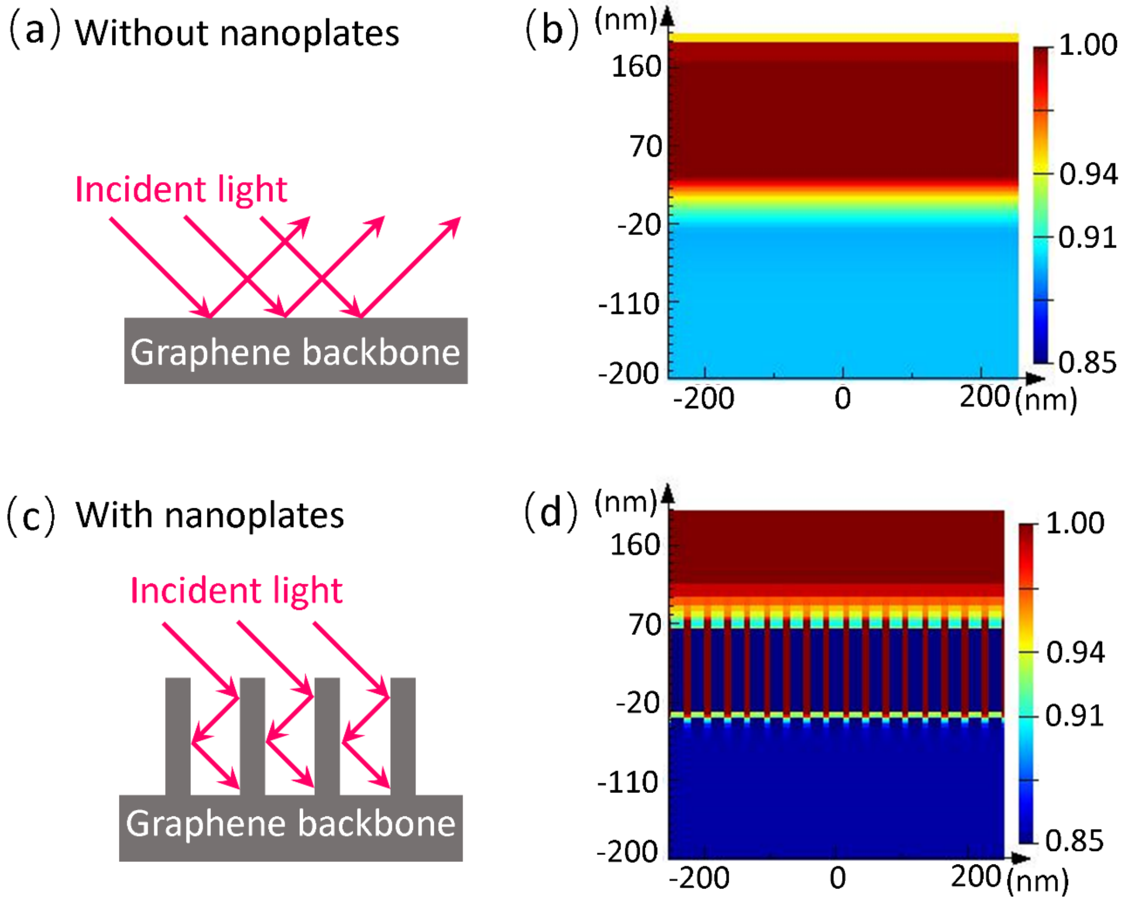

Fig. S4 (a) Absorption spectrum of the PEDOT:PSS film. (b) Light spectrum of the light source for the solar illumination in the experiments.

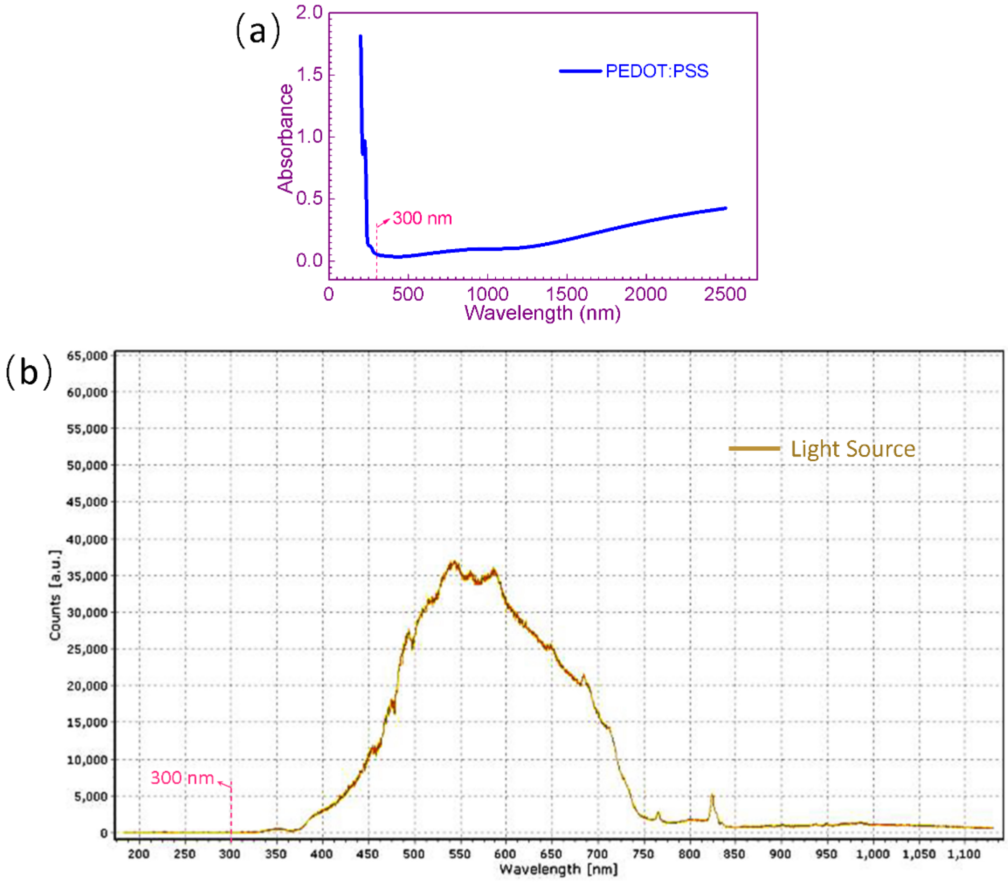

Fig. S5 Dependence of the IR drop and corresponding internal resistance on the photothermal temperature and heating temperature. (a) Dependence of the IR drop on the photothermal temperature and heating temperature. Note that the galvanostatic charge/discharge (GCD) current density is 3.3 mA cm^{-3}. (b) Dependence of the internal resistance obtained from the IR drop on the photothermal temperature and heating temperature.

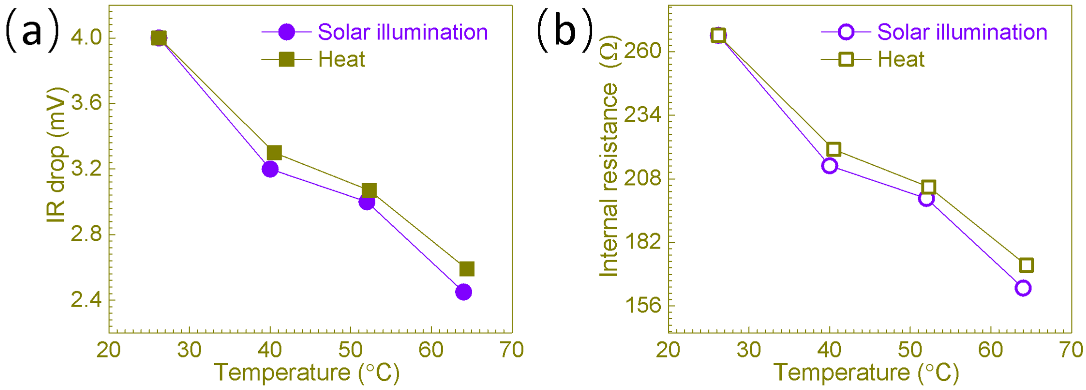

Fig. S6 Cycle tests of the supercapacitor in dark and under 1 solar illumination. (a) Retention test of the supercapacitor in dark (~25 °C) via continuous GCD cycling process. The inset shows the GCD curves from the 15080th to the 16000th cycle. (b) Retention test of the supercapacitor under 1 solar illumination via continuous GCD cycling process. The inset shows the GCD curves from the 1080th to the 2000th cycle.

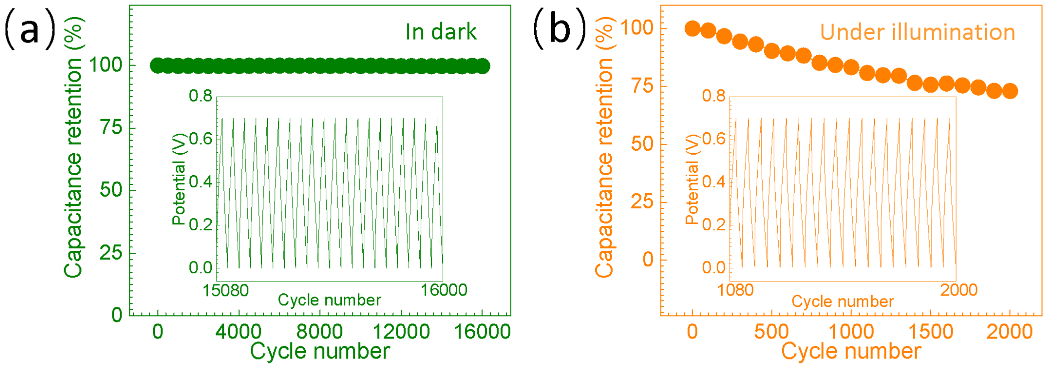

Fig. S7 (a) The galvanostatic charge/discharge (GCD) curves of the pseudo-type supercapacitor stays under 1 solar illumination before and after 2.5 h. (b) The GCD curves of the pseudo-type supercapacitor stays heated at 62°C before and after 2.5 h. (c) The GCD curves of the double-layer-type supercapacitor stays under 1 solar illumination before and after 2.5 h. (d) The GCD curves of the double-layer-type supercapacitor stays heated at 62°C before and after 2.5 h.

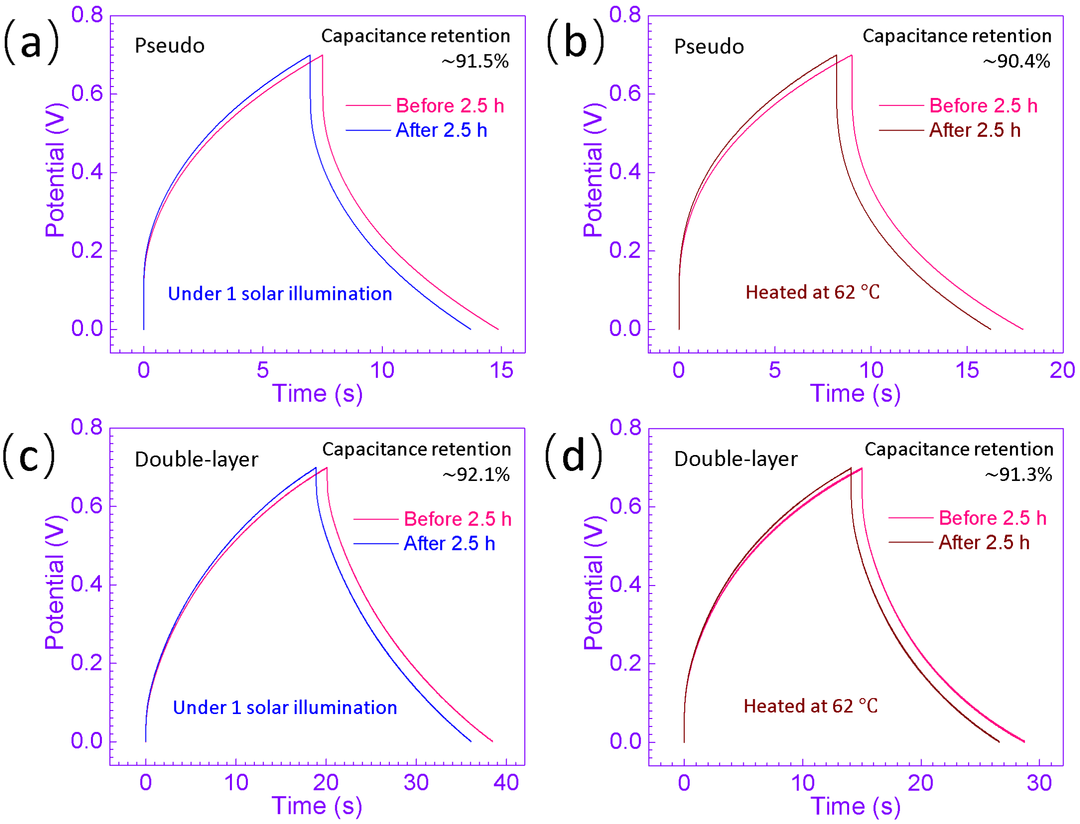

Fig. S8 (a-b) Photographs showing the solid-state PVA/H_3PO_4 electrolyte (a) in the original condition and (b) after staying heated at 62 ℃ for 2.5 h. (c-e) SEM images of the supercapacitor electrode filled with solid-state PVA/H_3PO_4 electrolyte (c) in the original condition, (d) after 2000 continuous cycles of GCD test under 1 solar illumination and (e) after 2000 continuous cycles of GCD test under heated at 63 °C. (f) FTIR spectra of the supercapacitor electrode filled with solid-state PVA/H_3PO_4 electrolyte in the original condition; after 2000 continuous cycles of GCD test under 1 solar illumination or heated at 63 °C. (Peak 1: 828 cm^{-1}; Peak 2: 980 cm^{-1}; Peak 3: 1090 cm^{-1})

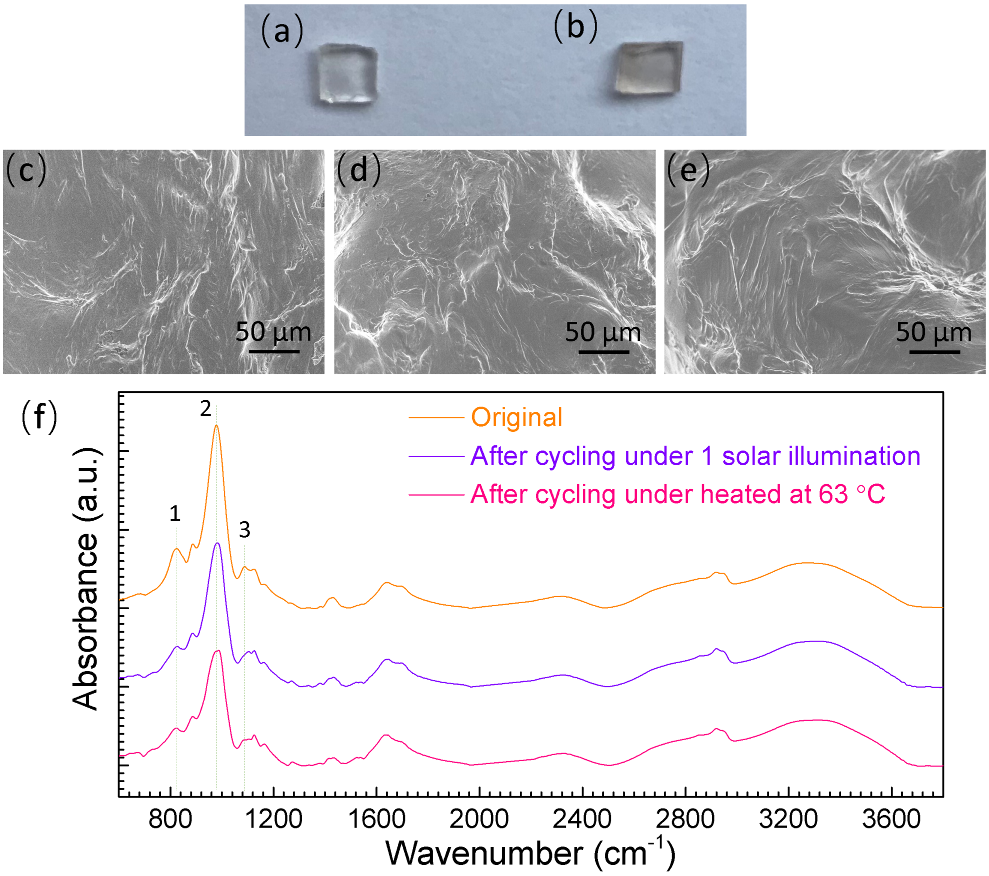

Fig. S9 Dielectric constants of the solid-state PVA/H_3PO_4 electrolyte at different temperatures before and after staying under 1 solar illumination or heated at 62 ℃ for 2.5 h.

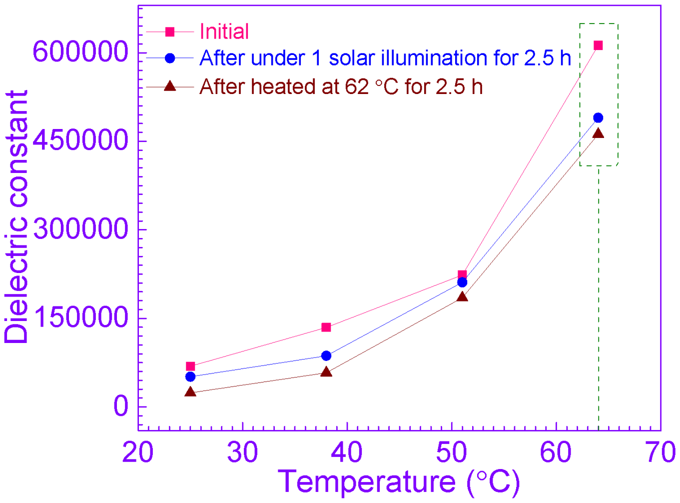

Fig. S10 Coulombic efficiencies of the supercapacitor under various light illumination intensities and at various heating temperatures. (a) Coulombic efficiencies of the supercapacitor at different GCD current densities under various light illumination intensities. (b) Coulombic efficiencies of the supercapacitor at different GCD current densities under various heating temperatures.

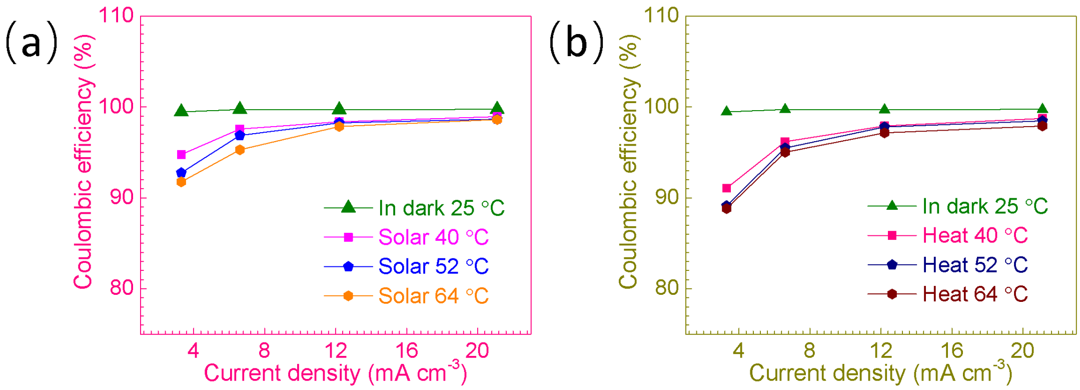

Note that the coulombic efficiency of the supercapacitor is defined as the ratio of the charge delivered during the discharge to that stored during the charge:

$$\eta = \frac{t_d}{t_c} \times 100\% \tag{S46}$$

where t_d and t_c are the time required for the discharging and charging processes respectively.

Fig. S11 The cyclic voltammetry (CV) curves of the supercapacitor upon periodic dark/illumination cycles.

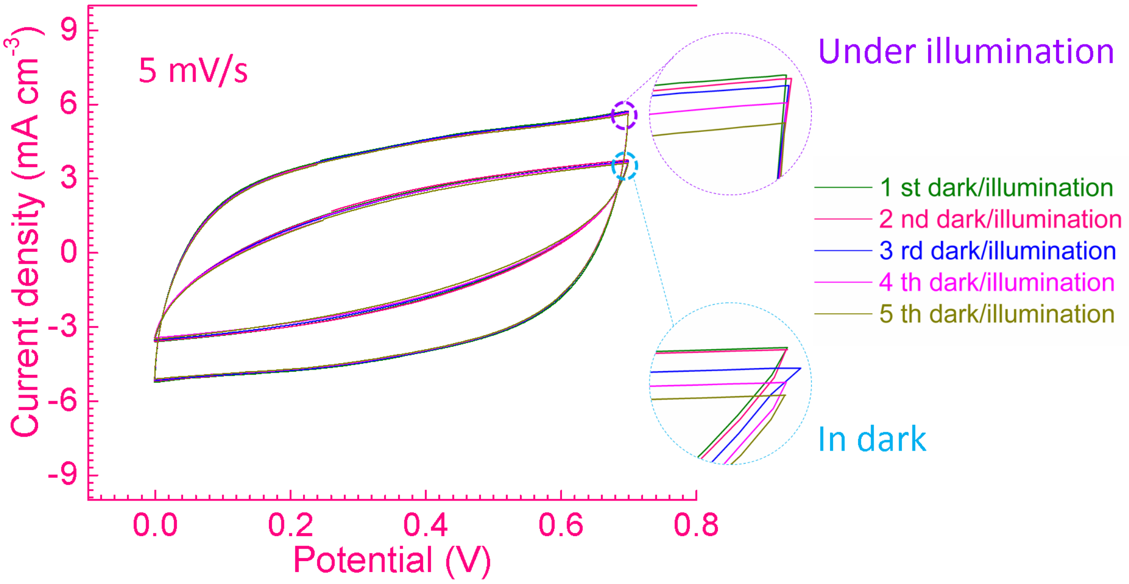

Fig. S12 CV and GCD curves of the supercapacitor under various light illumination intensities. (a-d) The CV curves at a scan rate of (a) 10 mV s^{-1}, (b) 20 mV s^{-1}, (c) 50 mV s^{-1}, and (d) 100 mV s^{-1} of the supercapacitor under various light illumination intensities. (e-g) The GCD curves at a current density of (e) 6.7 mA cm^{-3}, (f) 12.2 mA cm^{-3}, and (g) 21.1 mA cm^{-3} of the supercapacitor under various light illumination intensities.

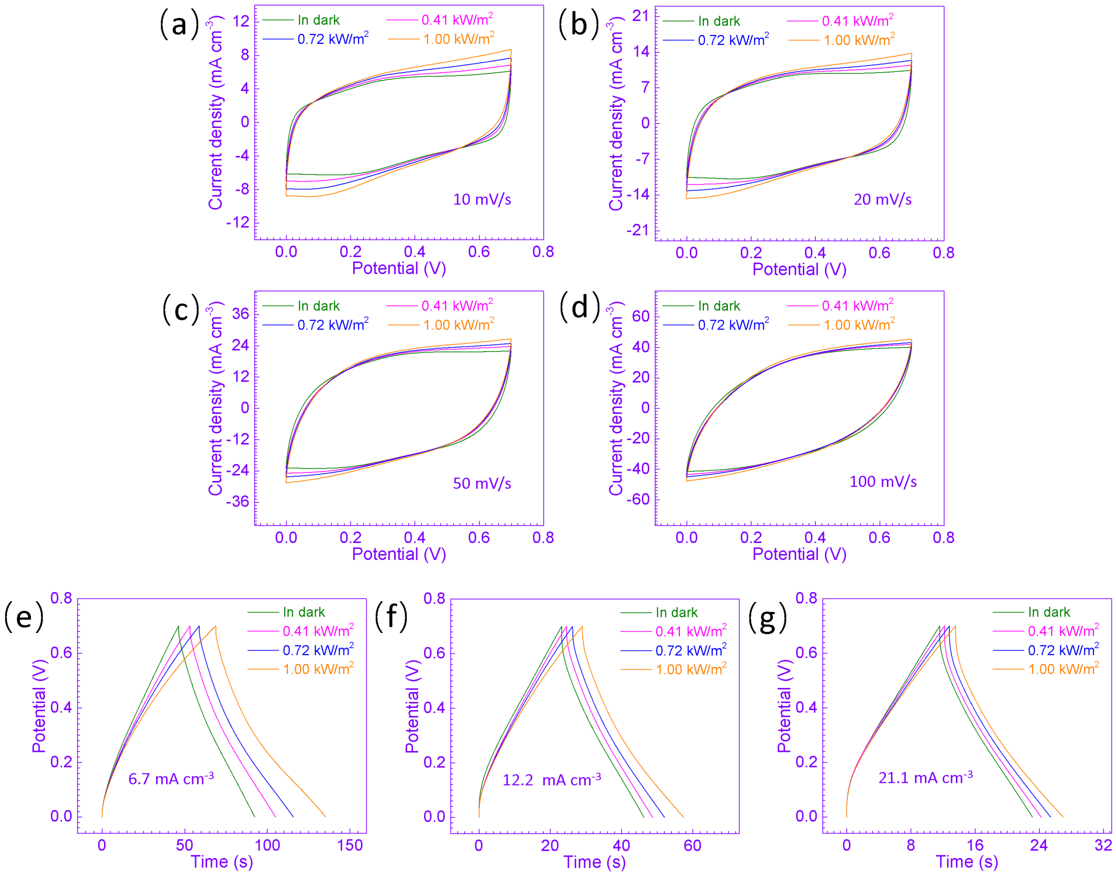

Fig. S13 Dependence of the equivalent series resistance (R_{esr}) and ionic resistance on the photothermal temperature and heating temperature. (a) Dependence of the R_{esr} obtained from the EIS curve on the photothermal temperature and heating temperature. (b) Dependence of the ionic resistance obtained from the EIS curve on the photothermal temperature and heating temperature.

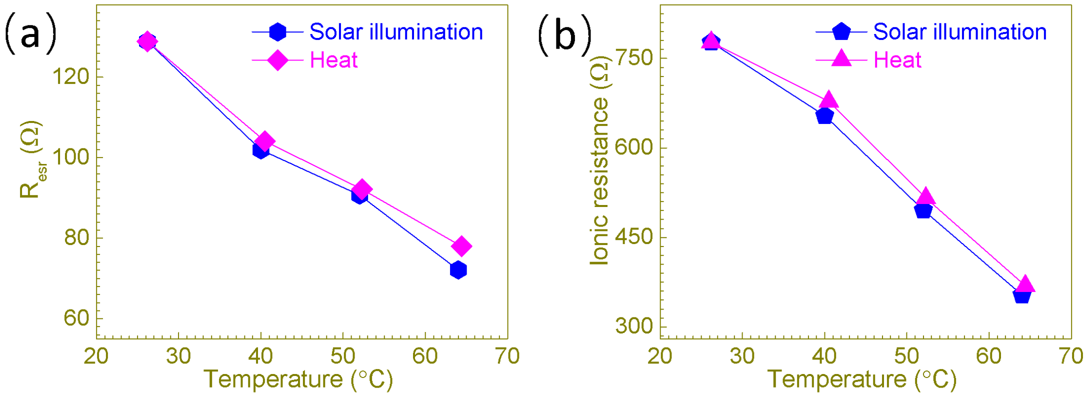

Fig. S14 Influences of solar power density on the electrode conductivity and electrolyte conductivity. (a) Relationship between the electrode conductivity and solar power density. (b) Relationship between the electrolyte conductivity and solar power density.

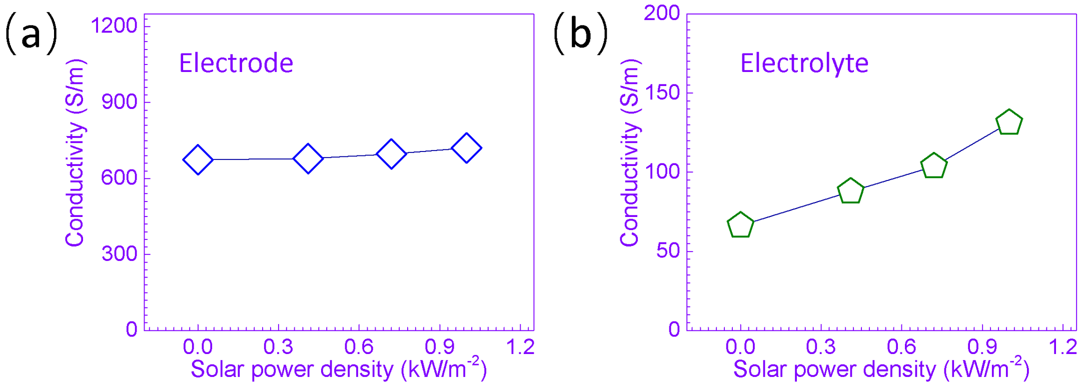

Fig. S15 Electrochemical properties of the double-layer-type supercapacitor (EDLC) in dark and under 1 solar illumination. (a-b) CV curves at various scan rates for the EDLC (a) in dark and (b) under 1 solar illumination. (c) Comparative CV curves at 5 mV s^{-1} of the EDLC in dark and under 1 solar illumination. (d-e) GCD curves at various current densities of the EDLC (d) in dark and (e) under 1 solar illumination. (f) Comparative GCD curves at 1.0 mA cm^{-3} of the EDLC in dark and under 1 solar illumination. (g-h) Volumetric specific capacitances calculated from the (g) CV curves and (h) GCD curves. (i) Coulombic efficiencies of the EDLC in dark and under 1 solar illumination.

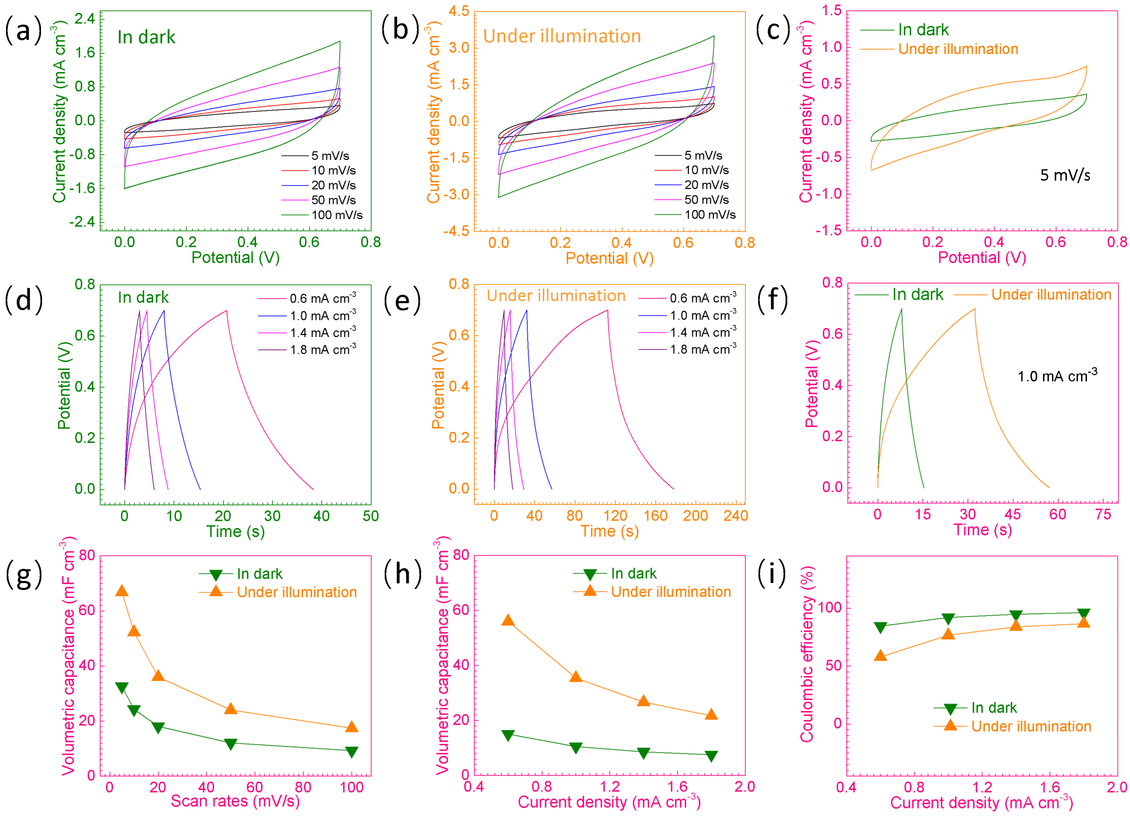

Fig. S16 Dependences of the pseudo-type supercapacitor capacitance and electric double-layer capacitance on the photothermal temperature. (a) Dependence of the pseudo-type supercapacitor capacitance (total capacitance) on the photothermal temperature by solar illumination. (b) Dependence of the double-layer-type supercapacitor capacitance (EDLC capacitance) on the photothermal temperature by solar illumination.

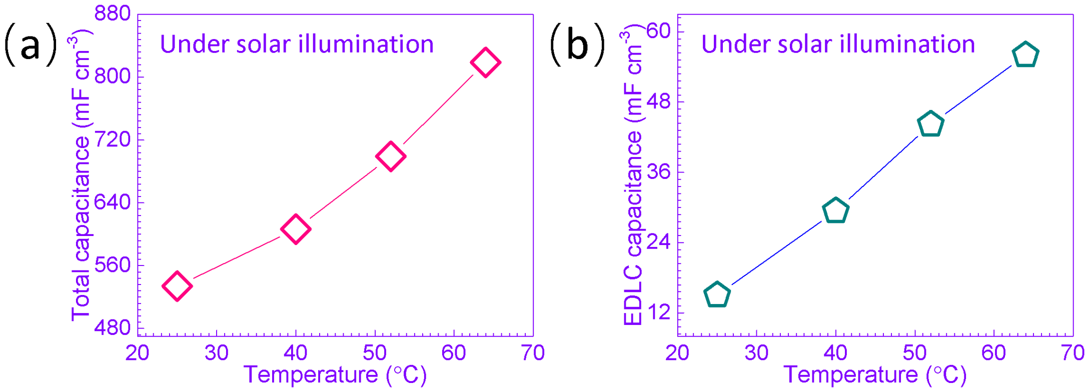

Fig. S17 Influence of the temperature on the dielectric constant of the PVA/H_3PO_4 electrolyte and simulated relationship between the EDLC capacitance and temperature. (a) Influence of the temperature on the dielectric constant of the solid-state PVA/H_3PO_4 electrolyte (frequency: 100 Hz). (b) Simulation results for the relationship between the EDLC capacitance and temperature. Note that the simulation was carried out by a classical EDLC model based on plane electrodes.

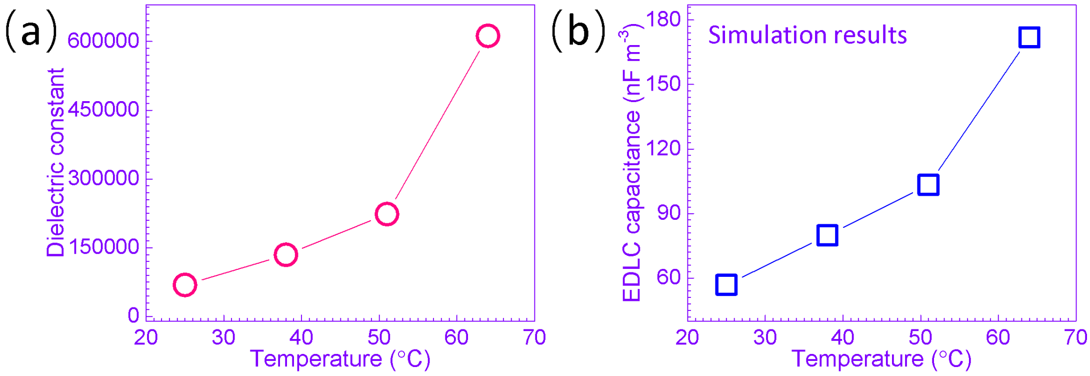

Fig. S18 Simulated electrolyte concentration distributions and GCD curves in dark upon changing the diffusion coefficient. (a) Simulated results for the evolution of electrolyte concentration gradient with the increasing charging potential of the supercapacitor in dark (diffusion coefficient: 1.18 $\times 10^{-15}$ m^2/s). (b-c) Simulated result for the electrolyte concentration gradient at 0.7 V with a diffusion coefficient of (b) 1.18 $\times 10^{-12}$ m^2/s and (c) 1.18 $\times 10^{-11}$ m^2/s. (d) Simulated GCD curves (current density: 6.7 mA cm^{-3}) of the supercapacitor in dark with various diffusion coefficients.

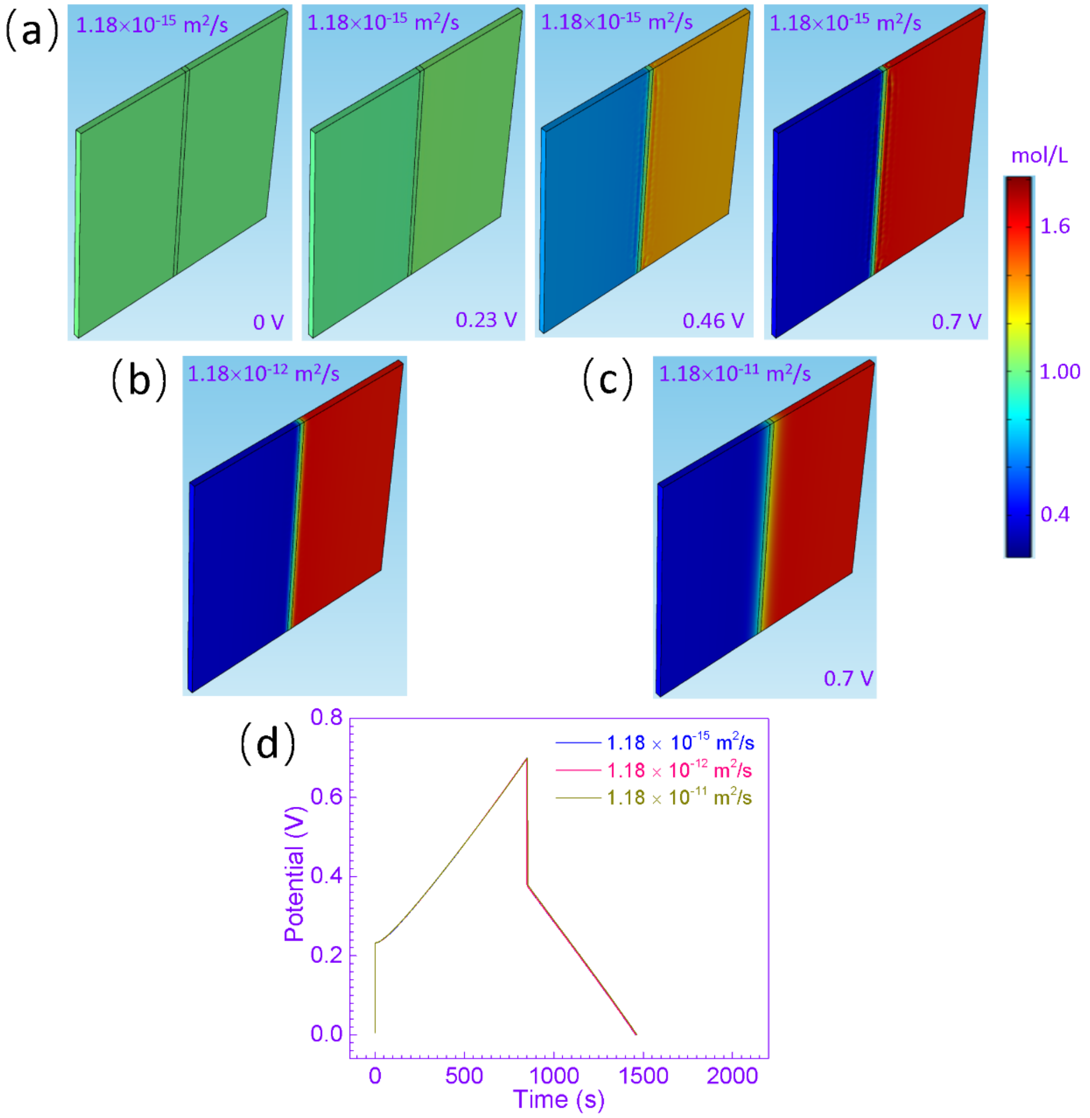

Fig. S19 Simulated GCD curves in dark upon changing the reaction rate constant and dependence of the capacitance on the reaction rate constant. (a) Simulated GCD curves (current density: 6.7 mA cm^{-3}) of the pseudo-type supercapacitor in dark with various reaction rate constants. (b) Simulated results for the relationship between the reaction rate constant and capacitance of the pseudo-type supercapacitor. (c) The values of the reaction rate constant at different photothermal temperatures fitted by the Arrhenius equation.

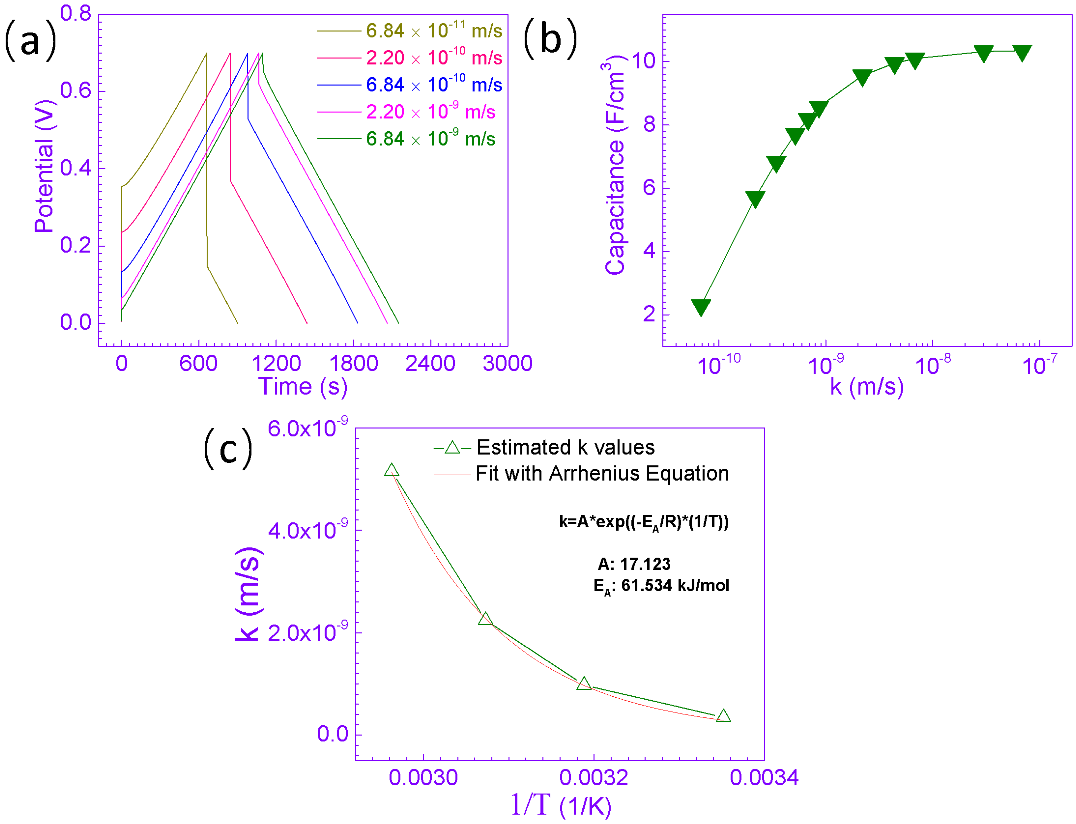

Fig. S20 (a) Simulated GCD curves (6.7 mA cm^{-3}) of the supercapacptior at different photothermal temperatures. (b) Simulated GCD curves showing contributions of variables to the enhanced capacitance.

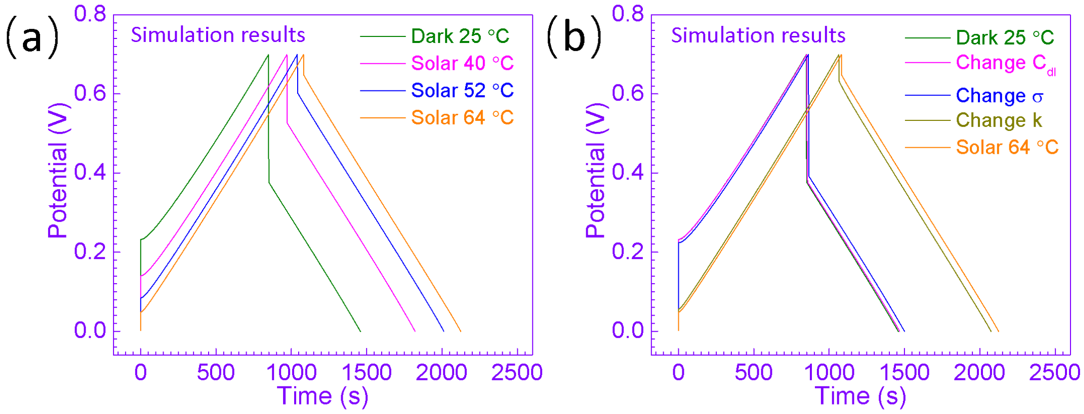

Fig. S21 Retention test of the supercapacitor under heated at 63 ℃ via continuous GCD cycling process. The inset shows the GCD curves from the 1080th to the 2000th cycle.

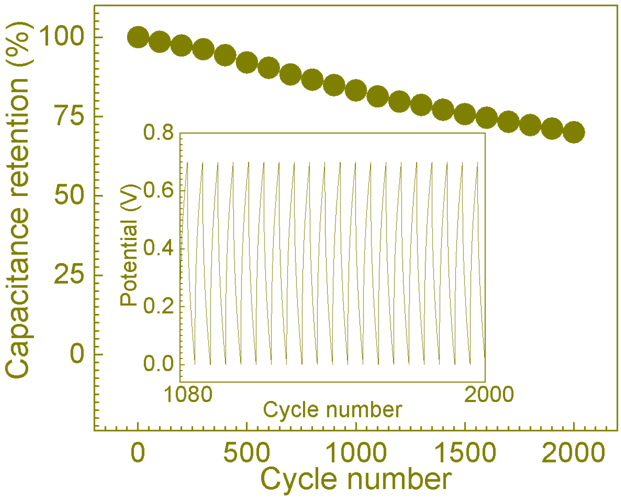

Fig. S22 Absorbance spectrum of the supercapacitor in the visible light range and simulated temperature distributions. (a) Absorbance spectrum of the supercapacitor in the visible light range. (b-d) Simulation results showing the temperature difference between the top and bottom surface of the 3D graphene at (b) solar 40.5 °C, (c) solar 52.3 °C, and (d) solar 64.4 °C. (e-g) Simulation results showing the temperature difference between the top and bottom surface of the solid-state PVA/H_3PO_4 electrolyte at (e) solar 40.5 °C, (f) solar 52.3 °C, and (g) solar 64.4 °C.

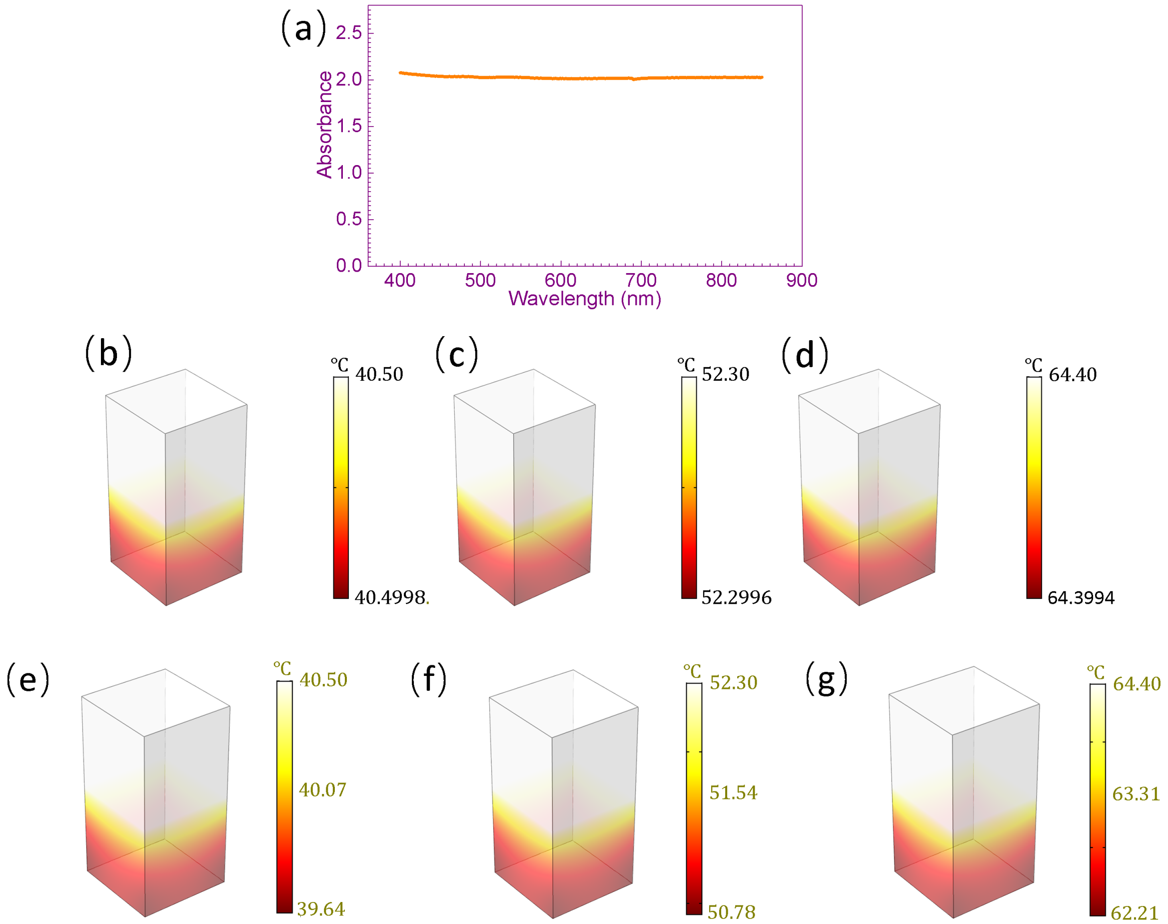

Fig. S23 Plots of $I_{(V=0.7\ V)}/\upsilon^{1/2}$ against $\upsilon^{1/2}$ based on the CV curves at different scan rates of the pseudo-type supercapacitor.

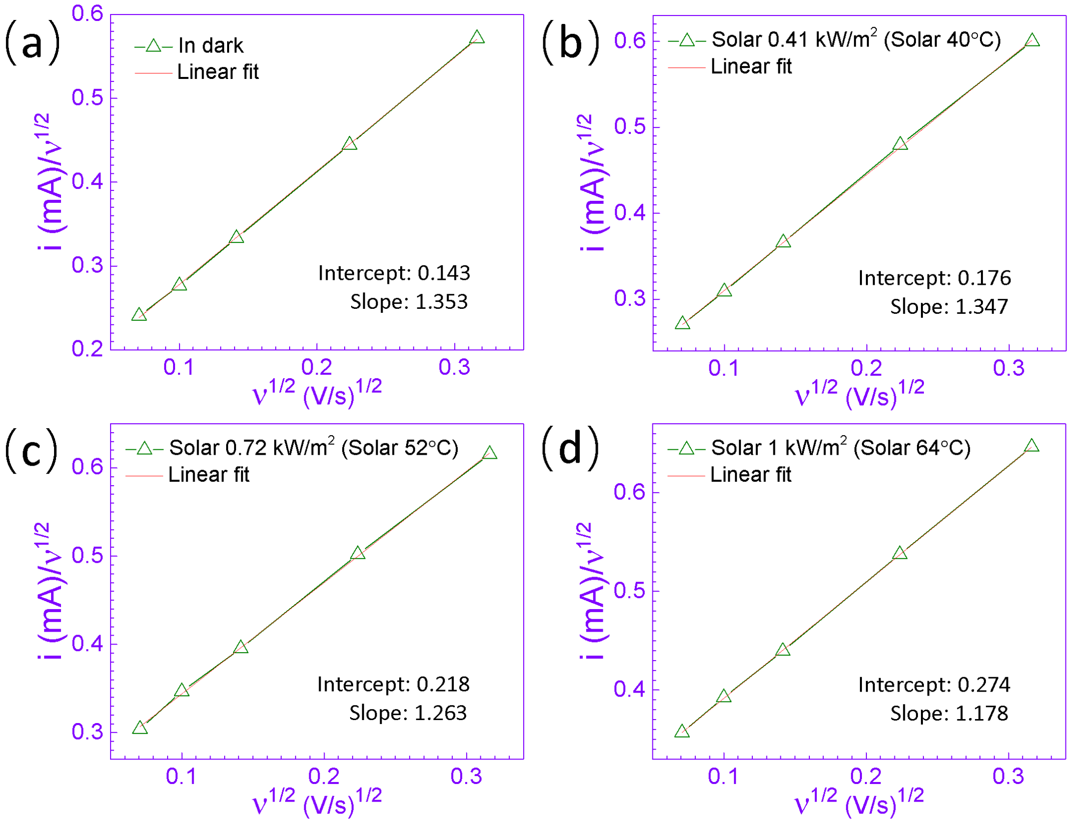

References

1 C. M. Hessel, V. P. Pattani, M. Rasch, M. G. Panthani, B. Koo, J. W. Tunnell and B. A. Korgel, *Nano Lett.*, 2011, **11**, 2560-2566.

2 H. K. Raut, V. A. Ganesh, A. S. Nair and S. Ramakrishna, *Energy Environ. Sci.*, 2011, **4**, 3779-3804.

3 J. Wang, Y. Li, L. Deng, N. Wei, Y. Weng, S. Dong, D. Qi, J. Qiu, X. Chen and T. Wu, *Adv. Mater.*, 2017, **29**, 1603730.

4 D. K. Roper, W. Ahn and M. Hoepfner, *J. Phys. Chem. C*, 2007, **111**, 3636-3641.

5 M. Banks, J. R. Ebdon and M. Johnson, *Polymer*, 1993, **34**, 4547-4556.

6 V. Pupkevich, V. Glibin and D. Karamanev, *J. Power Sources*, 2013, **228**, 300-307.

7 C. N. R. Rao, *Chemical applications of infrared spectroscopy*, Academic Press, New York, 1963.

8 J. Haslam and H. A. Willis, *Identification and analysis of plastics*, Iliffe Books Ltd., 1965.

9 M. Suzuki, T. Yoshida, T. Koyama, S. Kobayashi, M. Kimura, K. Hanabusa and H. Shirai, *Polymer*, 2000, **41**, 4531-4536.

10 F. Zhan, M. Liu, M. Guo and L. Wu, *J. Appl. Polym. Sci.*, 2004, **92**, 3417-3421.
11 F. Ahmad and E. Sheha, *J. Adv. Res.*, 2013, **4**, 155-161.
12 B. Łaszkiewicz, *J. Appl. Polym. Sci.*, 1971, **15**, 437-443.
13 N. Inagaki, K. Tomiha and K. Katsuura, *Polymer*, 1974, **15**, 335-338.
14 B. E. Conway, *Electrochemical supercapacitors: scientific fundamentals and technological applications*, Plenum Publishers, New York, 1999.
15 N.-S. Choi, Z. Chen, S. A. Freunberger, X. Ji, Y.-K. Sun, K. Amine, G. Yushin, L. F. Nazar, J. Cho and P. G. Bruce, *Angew. Chem., Int. Ed.*, 2012, **51**, 9994-10024.
16 D. Puthusseri, V. Aravindan, S. Madhavi and S. Ogale, *Energy Environ. Sci.*, 2014, **7**, 728-735.
17 X. Xia, Y. Zhang, D. Chao, Q. Xiong, Z. Fan, X. Tong, J. Tu, H. Zhang and H. J. Fan, *Energy Environ. Sci.*, 2015, **8**, 1559-1568.
18 C. Li, X. Zhang, K. Wang, X. Sun, G. Liu, J. Li, H. Tian, J. Li and Y. Ma, *Adv. Mater.*, 2017, **29**, 1604690.
19 J. Newman and K. E. Thomas-Alyea, *Electrochemical systems, 3rd ed,* Hoboken: Wiley, 2004.
20 C. Hao, X. Wang, Y. Yin and Z. You, *J. Electron. Mater.*, 2016, **45**, 515-526.
21 C. Lin, J. A. Ritter, B. N. Popov and R. E. White, *J. Electrochem. Soc.*, 1999, **146**, 3168-3175.
22 C. Lin, B. N. Popov and H. J. Ploehn, *J. Electrochem. Soc.*, 2002, **149**, A167-A175.
23 H. Kim and B. N. Popov, *J. Electrochem. Soc.*, 2003, **150**, A1153-A1160.
24 R. E. White, S. E. Lorimer and R. Darby, *J. Electrochem. Soc.*, 1983, **130**, 1123-1126.
25 M. Doyle, J. Newman, A. S. Gozdz, C. N. Schmutz and J. M. Tarascon, *J. Electrochem. Soc.*, 1996, **143**, 1890-1903.
26 T. R. Jow and J. P. Zheng, *J. Electrochem. Soc.*, 1998, **145**, 49-52.
27 K. A. Smith, C. D. Rahn and C.-Y. Wang, *Energy Convers. Manage.*, 2007, **48**, 2565-2578.
28 Y. Zhang, H. He, Z. Yuan, S. Wang and X. Liu, *Int. J. Hydrogen Energy*, 2011, **36**, 2230-2236.
29 J. Newman and W. Tiedemann, *AIChE J.*, 1975, **21**, 25-41.
30 T. Brezesinski, J. Wang, S. H. Tolbert and B. Dunn, *Nat. Mater.*, 2010, **9**, 146.
31 V. Augustyn, P. Simon and B. Dunn, *Energy Environ. Sci.*, 2014, **7**, 1597-1614.
32 D. Chao, C. Zhu, P. Yang, X. Xia, J. Liu, J. Wang, X. Fan, S. V. Savilov, J. Lin, H. J. Fan and Z. X. Shen, *Nat. Commun.*, 2016, **7**, 12122.
33 C. Comminges, R. Barhdadi, M. Laurent and M. Troupel, *J. Chem. Eng. Data*, 2006, **51**, 680-685.
34 N. G. Tsierkezos, *J. Solution Chem.*, 2007, **36**, 289-302.
35 D. DeLongchamp and P. T. Hammond, *Adv. Mater.*, 2001, **13**, 1455-1459.
36 C. Lei, P. Wilson and C. Lekakou, *J. Power Sources*, 2011, **196**, 7823-7827.
37 A. J. Bard and L. R. Faulkner, *Electrochemical methods: fundamentals and applications*, John Wiley&Sons, New York, 1980.
38 F. Sundfors, J. Bobacka, A. Ivaska and A. Lewenstam, *Electrochim. Acta*, 2002, **47**, 2245-2251.
39 C. P. Cohen Stuart, *in: KNAW, Proceedings*, 1912, **14**, 1159-1173.
40 M. D. John, D. Michenfelder, and M. D. Richard, A. Theye, *Anesthesiology*, 1968, **29**, 1107-1112.
41 R. Myers, *The basics of chemistry,* Greenwood Publishing Group, 2003.
42 H. Wang, J. Fang and L. Pilon, *Electrochim. Acta*, 2013, **109**, 316-321.
43 J. H. Masliyah and S. Bhattacharjee, *Electrokinetic and colloid transport phenomena,* John Wiley&Sons, New York, 2001.

44 H. J. Butt and M. Kapple, *Surface and interfacial forces*, Wiley-VCH, Weinheim, Germany, 2010.

45 F. Chen and P. Liu, *ACS Appl. Mater. Interfaces*, 2011, **3**, 2694-2702.

46 M. S. Kilic, M. Z. Bazant and A. Ajdari, *Phys. Rev. E*, 2007, **75**, 021502.

47 M. Z. Bazant, M. S. Kilic, B. D. Storey and A. Ajdari, *Adv. Colloid Interface Sci.*, 2009, **152**, 48-88.

48 K. H. Kim, K. C. Park and D. Y. Ma, *J. Appl. Phys.*, 1997, **81**, 7764-7772.

49 E. Benamar, M. Rami, C. Messaoudi, D. Sayah and A. Ennaoui, *Sol. Energy Mater. Sol. Cells*, 1999, **56**, 125-139.

50 S. Bandyopadhyay, G. K. Paul and S. K. Sen, *Sol. Energy Mater. Sol. Cells*, 2002, **71**, 103-113.

51 F. Yi, Q. Liao, X. Yan, Z. Bai, Z. Wang, X. Chen, Q. Zhang, Y. Huang and Y. Zhang, *Phys. E (Amsterdam, Neth.)*, 2014, **61**, 180-184.